

Broadband Plasmon-Induced Transparency to a Electromagnetically Induced Absorption Conversion Metastructure Based on Germanium

Di-Di Zhu, You Lv, Si-Ying Li, and Hai-Feng Zhang*

A Germanium (Ge) metastructure with switching features from broadband plasmon-induced transparency (PIT) and electromagnetically induced absorption (EIA) is presented, which forms a broadband PIT through the near-field coupling between the localized plasmon resonance and the Mie resonance employing four gold cut wires as bright plasmon resonators and four C-shaped dielectric rings as dark plasmon resonators. A wide transparent window above 0.9 is achieved covering from 0.622 to 0.823 THz with a relative bandwidth of 27.8%. In addition, through phase modulation, a magnetic dipole is generated by the constructive interference of the near-field coupling of the three resonators to realize the PIT to EIA conversion. In addition, a grid-like metastructure is introduced to realize the PIT to EIA conversion by phase modulation. To enhance the EIA bandwidth, another layer of C-shaped reflection plate resonator is introduced to increase the dark mode loss, and a layer of frequency selective surface composed of cross-shaped resonators is also used. Thus under the dual effect, a wide absorption window above 0.75 is achieved covering from 0.647 to 0.756 THz with a relative bandwidth of 15.5%.

As an intrinsic quantum mechanical phenomenon accompanied by strong dispersion, EIT is expected to be useful in areas such as quantum switching,^[12] photon storage,^[13] four-wave mixing,^[14] and regulations in light-pulse.^[15] The research history of EIT has spanned a century, and the first real experimental phenomenon of EIT was observed in a three-energy atomic system as early as 1991 by Boiler et al.^[16] However, the harsh experimental environment required to realize EIT, such as ultra-low temperature^[17] and high-intensity laser,^[18] seriously hinders the miniaturization of EIT devices and their application in practical engineering. In recent years, the rise of the so-called metastructures,^[5] that is, metamaterials and metasurfaces, have broken the bottleneck of EIT development. As subwavelength artificial periodic composites, metastructures have unique and


1. Introduction

Terahertz (THz) technology has been widely used in remote sensing, imaging, and biomedical diagnostics, gradually opening up a new era.^[1–3] Due to the characteristics of the frequency band in which THz is located, it also places higher demands on the design principles of devices and quasi-optical components.^[4] Electromagnetically induced transparency (EIT) is a quantum phase destructive interference phenomenon arising from alternative leap paths between ground and excited states in the triatomic energy level,^[5] which induces a sharp and narrow transmission window in opaque media.^[6–8] EIT is a highly resonant phenomenon that significantly slows down the incident electromagnetic wave velocity^[9,10] while greatly exacerbating the dispersion variation in opaque media, resulting in a large group index (GI).^[11]

exotic physical properties, such as negative refraction^[19,20] and electromagnetic polarization manipulation,^[21–23] which have become the "favorites" of many laboratories. To further miniaturize EIT-related devices, plasmon-induced transparency (PIT) has been proposed. PIT is a photo-induced oscillation of free electrons at the metal/dielectric interface, which exhibits strong optical confinement and extends the application of EIT to terahertz and optical wavelengths. However, similar to EIT, the narrow transparent window bandwidth has been a common drawback of the reported PIT effect schemes, which limits the development of technologies such as optical communication. Although Wu et al.^[24] proposed and demonstrated that increasing the number of layers of the PIT structure can effectively increase the bandwidth, the complex structure of 41 layers also leads to a huge fabrication challenge.

At the same time, with the rise of research in high-frequency fields such as THz, the drawback that metal resonators can trigger large non-radiative Joule losses has become more severe. As a result, various methods to reduce the losses and improve the Q-factor have been continuously investigated and demonstrated. One of the feasible strategies is to explore higher-order plasma surface lattice resonance.^[25,26] It has been shown that excitation of higher-order multi-poles,^[27] Mie resonances,^[28] toroidal resonances,^[29] Fano resonance,^[30] anapole modes,^[31] and Tamm resonances are effective in improving the Q-factor and reducing the radiation loss. The introduction of high-dielectric

D.-D. Zhu, Y. Lv, S.-Y. Li, H.-F. Zhang
College of Electronic and Optical Engineering & Flexible Electronics
(Future Technology) of Microelectronics
Nanjing University of Posts and Telecommunications (NJUPT)
Nanjing 210023, P. R. China
E-mail: hanlor@njupt.edu.cn

 The ORCID identification number(s) for the author(s) of this article can be found under <https://doi.org/10.1002/andp.202200425>

DOI: 10.1002/andp.202200425

constant dielectric resonators provides a solution to the problem of metal radiation loss at high frequencies by replacing the high-loss ohmic currents generated by metal resonators with low-loss displacement currents generated by dielectric resonators. At the same time, the large Q-factor difference between the metal and dielectric resonators fits well with the PIT bright-dark mode theory. However, metastructure system studies combining these two properties for PIT metastructure, especially for broadband properties, are still rare.

As a complementary effect to EIT, electromagnetic induction absorption (EIA) defines a band in which enhanced atomic absorption due to wave coherence can be observed.^[32] Although the EIT effect has been extensively studied, research on EIA is still in the process of development. EIA will open new paths for the design of new photonic devices in narrow-band filtering, absorption switching, and light modulators.^[33] It is reported that Tassin et al.^[34] introduced a radiative dual oscillator model to describe the absorption and scattering properties to achieve the transition from EIT to EIA by reducing the dissipative damping of the bright resonant cavity and increasing the dissipative damping of the dark resonant cavity. In addition, reducing the coupling strength between the bright and dark resonant cavities (e.g., increasing the coupling distance)^[35] and the different phases involved in the oblique incidence can also achieve the EIT to EIA transition.^[36] Among them, phase-shift modulation is an excellent way to achieve EIT/EIA switching,^[37,38] and the EIA phenomenon can be achieved in a multi-radiative metastructure by increasing the number of radiative states to produce interference between three and more excitation paths.

However, the reported EIA studies all exhibit sharp absorption bands, and studies of broadband EIA have not been reported, which limits the development of optoelectronic communication devices. Meanwhile, many EIT/EIA metastructures have been extensively studied, but little effort has been devoted to the combination and automatic switching of the two in a single device to meet complex engineering requirements (e.g., by varying external factors such as light and temperature to achieve the transition from optical transmission to absorption). At the same time, the frequency selective surface (FSS) has become a research hotspot as a favorable means of regulating electromagnetic waves. FSS is composed of a large number of resonant units arranged on a dielectric plate according to a certain rule,^[39] which is commonly used in radar radome and antenna sub-reflective surfaces. However few studies have combined the advantages of FSS with PIT/EIA metastructure.

In this paper, a Germanium (Ge) metastructure (GMST) with switching features from broadband PIT to EIA is presented. GMST forms a broadband PIT through the near-field coupling between the localized plasmon resonance and the Mie resonance employing four gold cut wires as bright plasmon resonators and four C-shaped dielectric rings as dark plasmon resonators. A wide transparent window above 0.9 is achieved covering from 0.622 to 0.823 THz with a relative bandwidth of 27.8%. In addition, a grid-like metastructure (GLM) is introduced to realize the PIT to EIA conversion by phase modulation. To enhance the EIA bandwidth, another layer of C-shaped reflection plate resonator (CRP) is introduced to increase the dark mode loss, and a layer of cross-shaped FSS resonator (CRFS) is also used. Thus under the dual effect, a wide absorption window above 0.75 with

Table 1. Detailed dimension.

Parameters	h_1	h_2	h_3	d_1	d_2	d_3	d_4
Value [μm]	32	6	10	1	1	27	1
Parameters	k_1	k_2	k_3	k_4	k_5	k_6	w_1
Value [μm]	60	10	5	10	5	180	128
Parameters	w_2	w_3	w_4	w_5	w_6	r_1	r_2
Value [μm]	8	71	8	10	115	25	36
Parameters	r_3	l_1	l_2	l_3	l_4	x	—
Value [μm]	30	240	170	100	10	100	—

a relative bandwidth of 15.5% is realized. In addition, the operating principle of GMST is explained by analyzing the surface current as well as the atomic energy level diagram, and the PIT and EIA phenomena are reproduced by using the circuit model to confirm the consistency and validity of the simulation and theory. This design is expected to provide new ideas for the design of electromagnetic induction switches with potential applications in the fields of radome design, optical delayers, and information coding.

2. The Design Process and Simulated Results

2.1. GMST Design

Figure 1a illustrates the top view of the proposed GMST cell structure. The meta-atoms include the top CRFSs, the middle layer four CPRs, and the bottom grid resonator GLM (all with integrated Ge). The GMST also has four gold (conductivity $\sigma_{\text{gold}} = 4.561 \times 10^7 \text{ S m}^{-1}$)^[40] cut wires and four C-shaped dielectric rings to form the PIT, as well as three dielectric spacers. It is noteworthy that the conductivity of the tunable material varies with the modulation of the external stimulus. The photosensitive semiconductor Ge can be excited by pump light at wavelengths less than 1800 nm,^[41] and the conductivity of Ge is assumed to be 0 S m^{-1} in the absence of pump beam illumination and gradually increases to $1 \times 10^6 \text{ S m}^{-1}$ with the peak of the pump beam power.^[41] As seen in **Figure 1b**, the dielectric spacer between the top CRFS and the middle layer CPR is transparent material PMMA (relative permittivity $\delta_{\text{PMMA}} = 2.5$, loss tangent $\tan\delta_{\text{PMMA}} = 0$)^[42] with a thickness of $h_3 = 10 \mu\text{m}$, which is introduced to facilitate the light to change the working state of the CPR. The remaining two layers are quartz substrates ($\delta_{\text{quartz}} = 3.793$, $\tan\delta_{\text{quartz}} = 0.0008$)^[23] with intermediate layer thickness $h_2 = 6 \mu\text{m}$ and bottom layer thickness $h_1 = 32 \mu\text{m}$. As shown in **Figure 1c–f**, the four C-shaped dielectric rings as dark plasmon resonators are composed of Titanium dioxide (TiO_2 , $\delta_{\text{TiO}_2} = 114$, $\tan\delta_{\text{TiO}_2} = 0.00027$)^[43] It constitutes eight dielectric rings with the upper CPR structure, and the upper and lower two constitute a group of four parts, each of which overlaps the central axis of the dielectric ring but differs 180° in the direction of the dielectric ring rotation. The centers of the four dielectric rings in two planes are connected to form a square with a side length of $x = 100 \mu\text{m}$. The detailed geometry of GMST is shown in **Table 1**. It is worth stating that the proposed GMST has a quadruple symmetry and has the same response results for the incident TE (electric field direction along y -direction, magnetic field direction along x -direction, wave vector

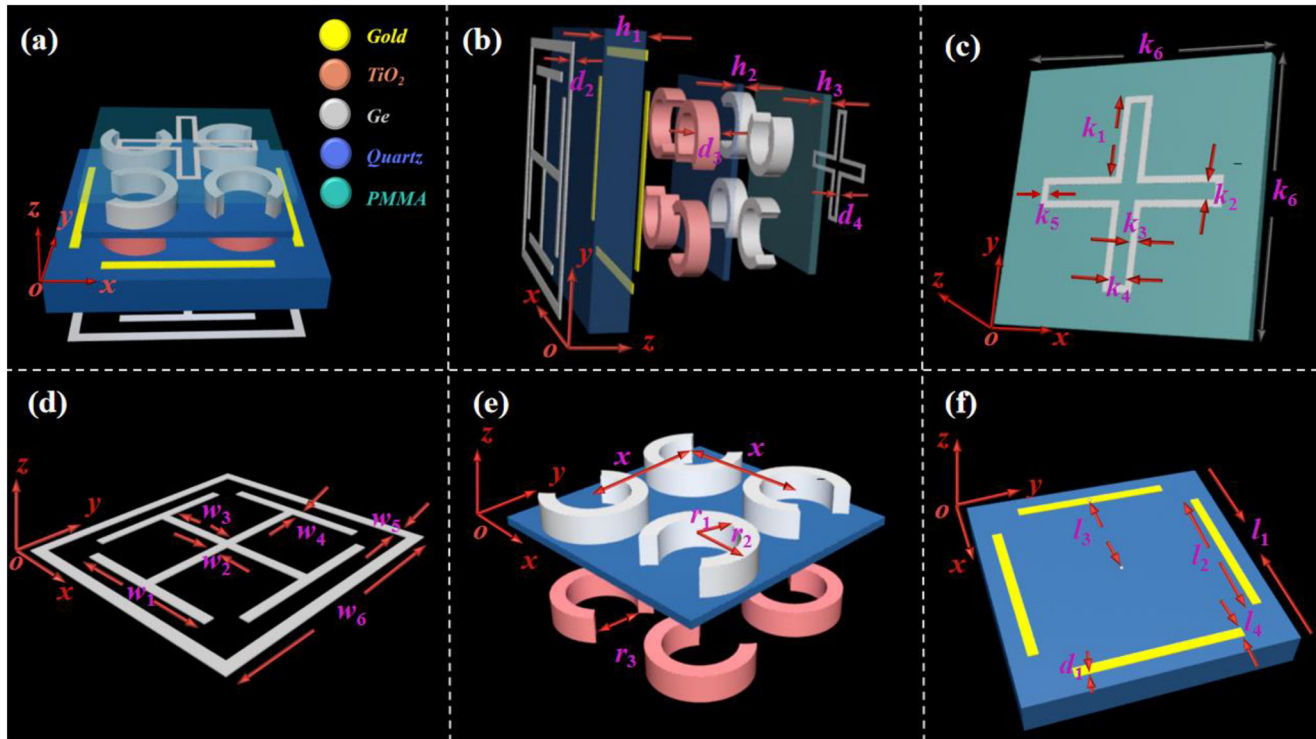


Figure 1. a) Top view of GMST, b) side view of GMST, c) CRFS structure diagram, d) GLM metastructure diagram, e) middle two-layer resonance (CPR and four C-shaped dielectric rings) structure diagram, and f) four gold cut wires schematic diagram.

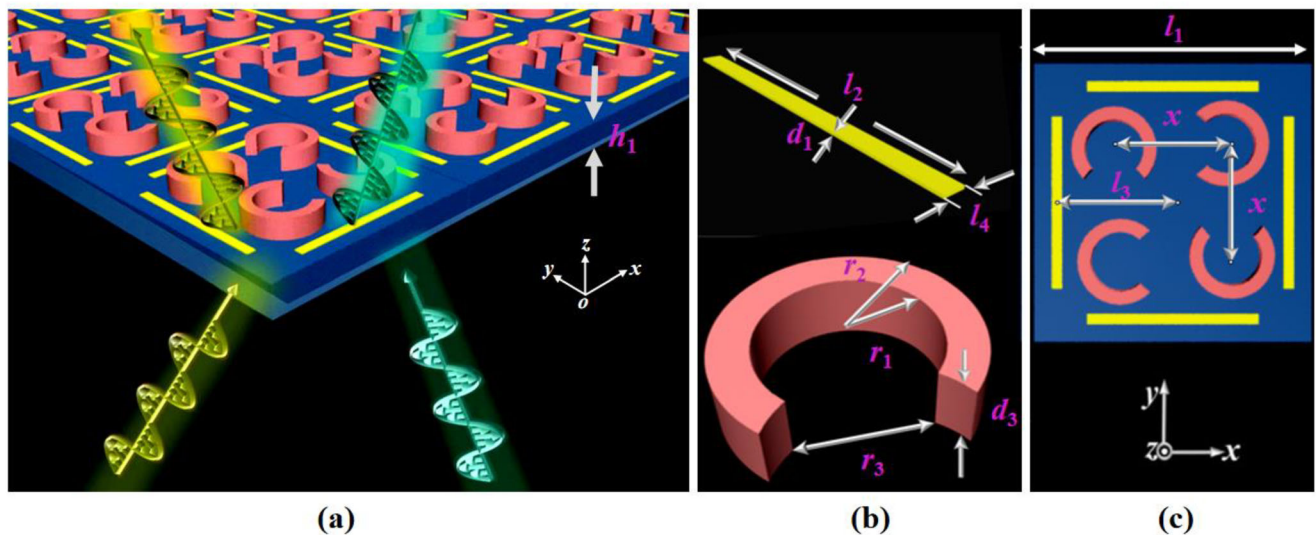


Figure 2. a) Array diagram forming the metastructure of the broadband PIT, b) a gold cut wire and a C-shaped dielectric ring diagram, and c) top view of PIT metastructure.

direction along z -direction) and TM (electric field direction along x -direction, magnetic field direction along y -direction, wave vector direction along z -direction) waves, that is, it has polarization insensitivity. The simulation results were obtained with the help of the commercial simulation software High Frequency Simulation Software (HFSS). The GMST are set up in close periodic

alignment in the simulation process (similar to **Figure 2a**), and the near-field coupling effects between adjacent unit cells (such as gold cut wires) are negligible and their effects have been considered in the experiments. The simulation results show that the formation principle and structural response results are the same for TM wave or TE wave incidence. Therefore, to observe the

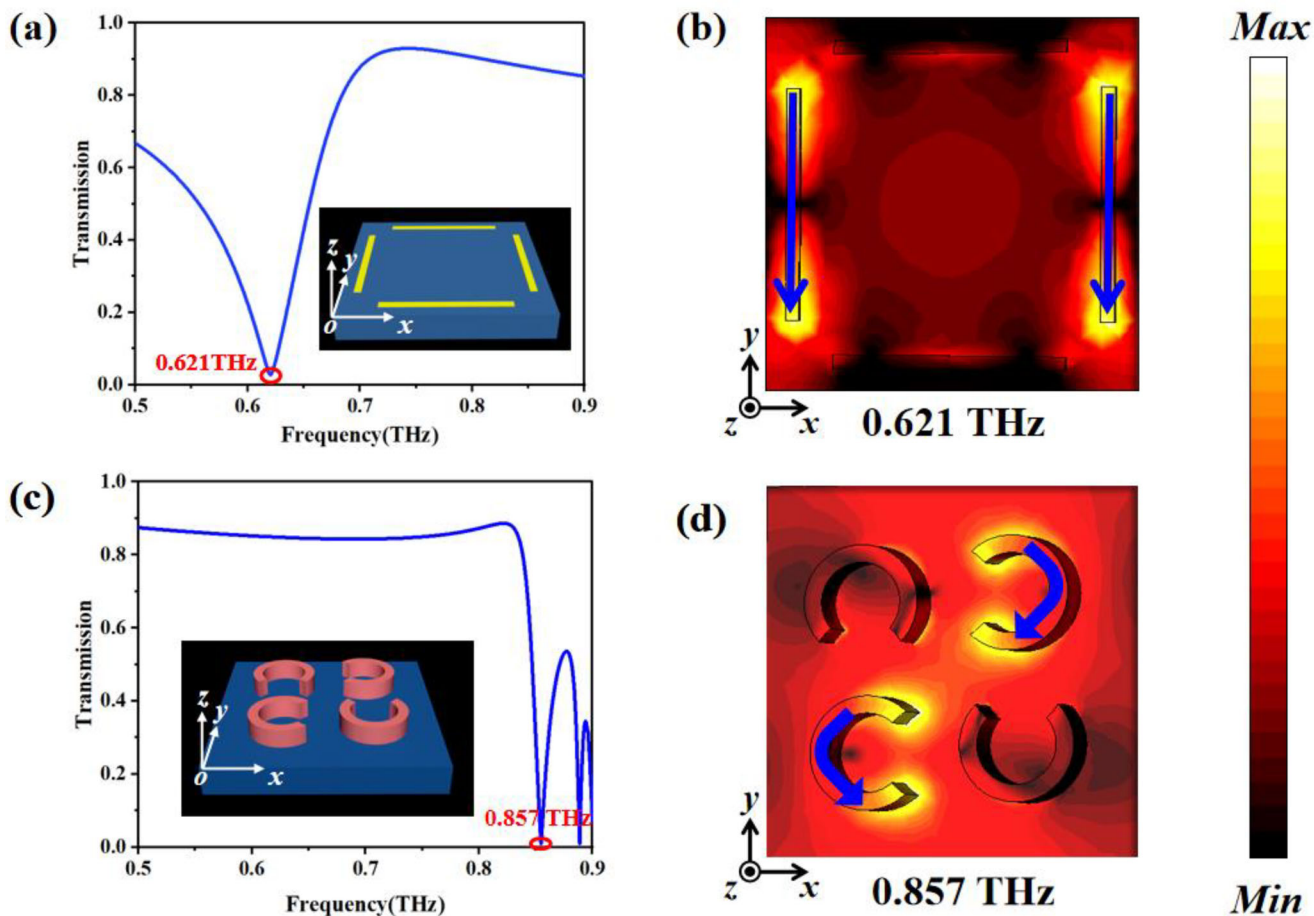


Figure 3. Four gold cut wires (bright plasmon resonators) resonate individually, a) transmission response curve, b) electric field distribution, and four C-shaped dielectric rings (dark plasmon resonators) resonate individually. c) transmission response curves, and d) electric field distribution.

phenomenon and explain the principle, TE wave incidence is used as an example in this paper.

2.2. PIT Mechanism Analysis

Figure 2 illustrates the periodic metastructure diagram of the first stage of forming a broadband PIT, consisting of four gold cut wires and four C-shaped dielectric rings on a quartz dielectric substrate (see Figure 2a for details). A schematic of the individual resonators and a plan view of the structure are shown in Figure 2b,c. Detailed dimensions can be found in Table 1. It should be emphasized that the proposed PIT metastructure has quadruple symmetry and the overall PIT metastructure is obtained by three 90° center rotations of a single resonator, and the PIT metastructure is polarization insensitive. **Figure 3a,c** shows the transmission curves of the separate responses of four gold cut wires and four C-shaped dielectric rings in TE mode, respectively. And the electric field diagrams corresponding to the two resonant frequency points are located in Figure 3b,d, respectively.

The two cut wires with the same radial direction as the incident electric field direction (y -direction) strongly excite the local surface plasmon resonance at 0.621 THz (see Figure 3a), and a

large amount of electric field energy is localized at both ends of the two gold cut wires (see Figure 3b), showing electric dipole properties, which can be used as a bright plasmon resonator. In this case, there is a strong coupling with free space, and at the same time, there is a large radiation loss, which is manifested in the transmission spectrum as a wide spectrum and a small Q value of 10.7 (quality factor $Q = f/\Delta f$ for the fundamental resonant mode, f is the resonant frequency and Δf denotes the half-peak bandwidth).^[44] As can be seen from Figure 3c,d, the two C-shaped dielectric rings with the notch linkage direction along the electric field direction can be directly excited by the incident electric field due to the asymmetry of the structure. The remaining two C-shaped dielectric rings are almost unresponsive and can only be excited indirectly, showing the magnetic dipole property, which is Mie resonance. Therefore, the weak coupling of the four C-shaped dielectric rings to the incident field is used as a dark plasmon resonator in this PIT metastructure. Comparing Figure 3a with Figure 3c, it can be seen that the dark resonator produces a high Q (42.9) resonance at 0.857 THz, which also proves the advantage of low loss under the action of displacement current. In summary, the bright and dark plasmon resonators satisfy the conditions for the generation of PIT, i.e., the difference in Q values between bright and dark modes is large and

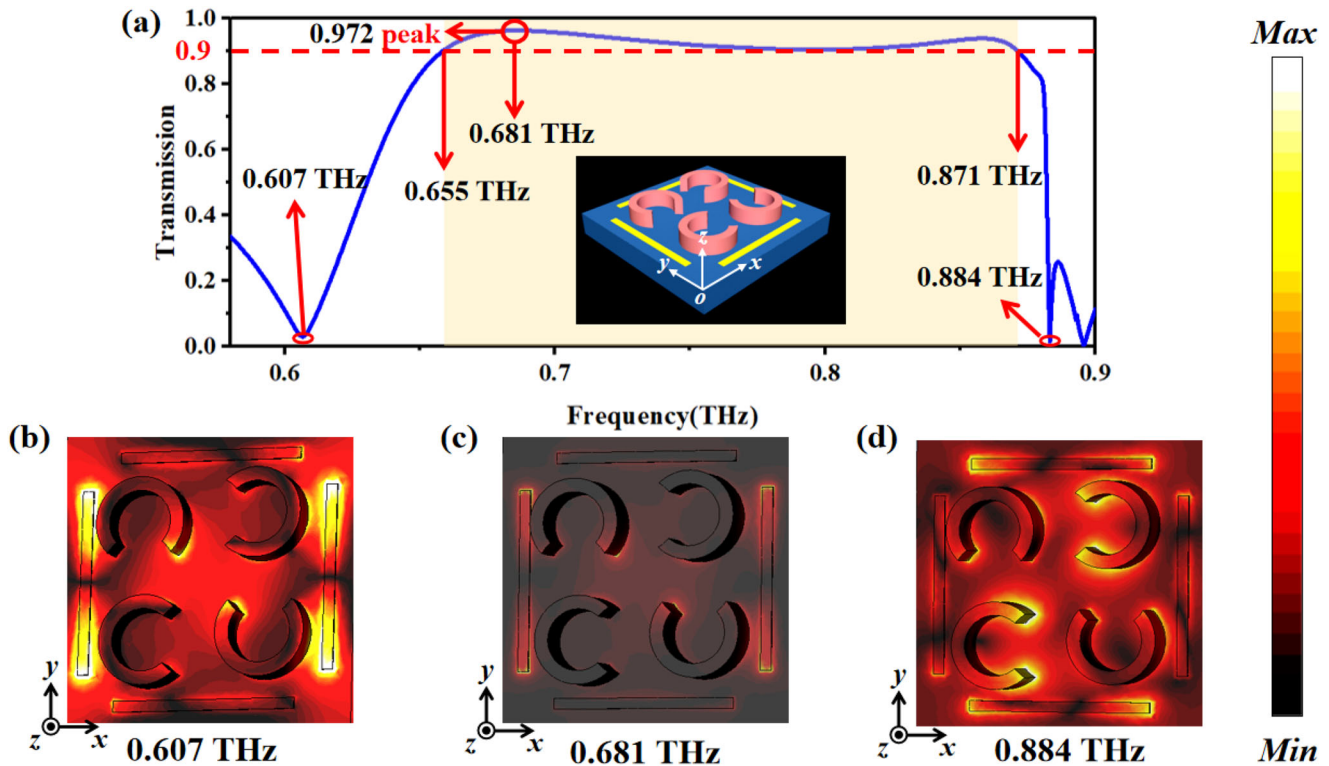


Figure 4. a) PIT transmission response curve, and electric field distribution chart, b) at 0.607 THz, c) at 0.607 THz, and d) at 0.607 THz.

the resonant frequency points are similar (0.621 and 0.857 THz, respectively). Therefore, when TE waves are incident, the phase destructive interference between the local surface plasmon resonance produced by four gold cut wires and the Mie resonance produced by four C-shaped dielectric rings leads to the PIT as displayed in **Figure 4a**, where the PIT metastructure produces transmission valleys at frequencies of 0.607 and 0.884 THz, and transmission peaks at 0.972 THz. Bright and dark plasmon resonators resonate individually at resonant frequencies very close to the two resonant frequencies of the complete PIT metastructure, while the transmission peak of the PIT metastructure lies between the two resonant frequencies, which is formed by the weak coupling between the two modes excited by the incident wave.

To illustrate this phenomenon, the electric field distribution at the transmission peak (0.681 THz) and the two transmission valleys (0.607 and 0.884 THz) are plotted in **Figure 4b–d**. It is easily observed that the accumulation of the electric field is caused by the self-coupling of the two gold cut wires coupled to the incident electric field in the radial direction along the electric field (y -axis), due to the self-coupling with the incident electric field, which causes a transmission depression at 0.607 THz. In contrast, the transmission valley at 0.884 THz is formed by the massive accumulation of electric field on two C-shaped dielectric rings, whose notch linkage is along the electric field (y -axis) direction. In addition, Through the near-field coupling between the localized plasmon resonance of the two gold cut wires and the Mie resonance of C-shaped dielectric rings, the large amount of electric field that originally gathered on the two gold cut wires due to direct excitation by the incident field was significantly suppressed,

which means the destructive interference similar to the classical three-level atomic system has been generated. Thus a wide transparency window above 0.9 is achieved covering from 0.655 to 0.871 THz with a relative bandwidth of 28.3%.

2.3. The Physical Mechanism of PIT Behavior

To facilitate the explanation of the PIT formation mechanism, **Figure 5** is plotted. PIT is a quantum interference phenomenon generated by two laser fields with detuned frequencies that interfere destructively with the spectrum of an atom that is otherwise in an absorbing state. That is, two different paths are required that interfere with each other and can lead to the same final atomic state. In the 3-level atomic systems (see **Figure 5a**), the two ground-state energy levels $|b\rangle$ and $|c\rangle$ are of similar energy and belong to the simplex energy level, while $|a\rangle$ is the excited state energy level. The probe electromagnetic wave operates at energy similar to $|b\rangle \rightarrow |a\rangle$, while another pump electromagnetic wave with very high energy can achieve $|c\rangle \rightarrow |a\rangle$, and the interference path is then generated by these two jumps. The familiar Lorentz absorption curve can be observed when the pump light laser is not operating. When the detection and pump light are operating simultaneously, both lasers are tuned to their respective atomic jumps, and there are two paths from energy level $|b\rangle$ to energy level $|a\rangle$: $|b\rangle \rightarrow |a\rangle$ and $|b\rangle \rightarrow |a\rangle \rightarrow |c\rangle \rightarrow |a\rangle$, with equal odds and opposite directions, and the interference effect of phase destructive interference occurs at energy level $|a\rangle$, making the atomic Bourget number at energy level $|a\rangle$ close to 0.^[45] The absorption is canceled due to phase destructive interference,

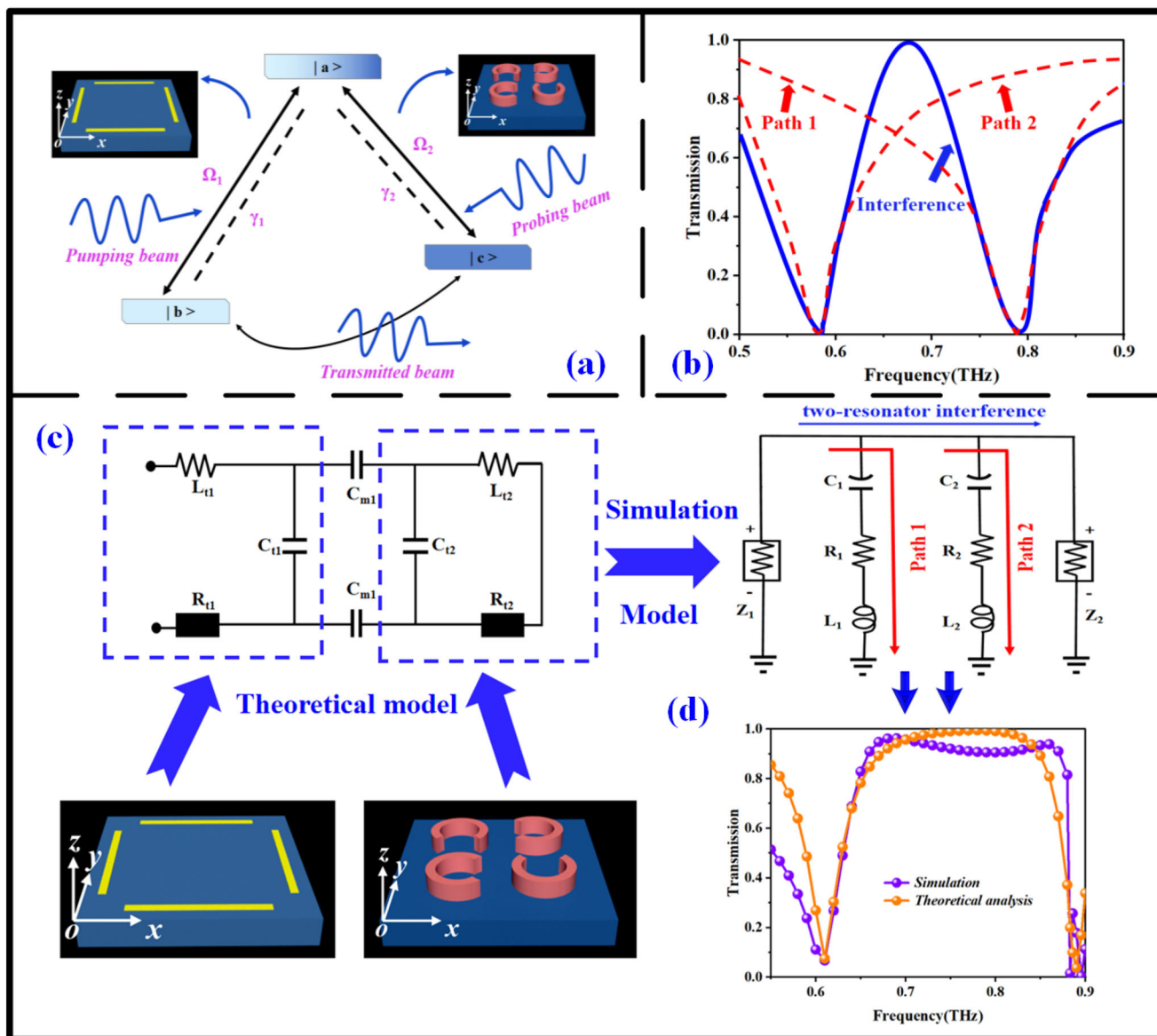


Figure 5. a) Explanation of the PIT phenomenon based on the 3-level atomic systems in TE mode, where γ_1 and γ_2 are the coupling coefficients between the energy levels, Ω_1 and Ω_2 are the transition phases. b) Formation of the theoretical transmission response curve of the PIT phenomenon. c) Explanation of the PIT phenomenon based on the circuit model, and d) comparison of the transmission response curve of the proposed PIT metastructure simulation with that of the circuit model theoretical analysis.

resulting in the PIT phenomenon. Establishing a circuit model of the coupled structure of the metastructure allows for a simpler understanding of the electromagnetic properties of the metastructure from the circuit perspective, and a more comprehensive analysis of the tuning of the metastructure properties from the perspective of the circuit parameters. The circuit approach to the analysis of metastructure requires a circuit model of the resonator. The simplest circuit model is to equate each resonator as an RLC in series. Here, the four gold cut wires and four C-shaped dielectric rings are respectively equated to an RLC circuit since the exact same resonator detuning frequency is the same. The loss of the resonator is equivalent to the resistance, the gap of the resonator is equivalent to the series capacitance, and the

resonator itself is equivalent to a coil that can be equated to a series inductor. The above equivalence is only the simplest way to obtain the RLC value, but in fact, the equivalent value of four gold cut wires and four C-shaped dielectric rings is much more complex and complicated. The equivalent value is closely related to the length, width, and height of the gold wires, the radii of the rings and the size of the opening, and the electromagnetic field frequency.^[46] The resonant frequency of each resonator can be derived from the equivalent capacitance and inductance values.

The theoretical equivalent circuit diagram of the PIT is shown in Figure 5c, where the two branch series RLC circuits represent the two bright and dark plasma resonators, respectively, and the coupling effect between the two resonators is represented by the

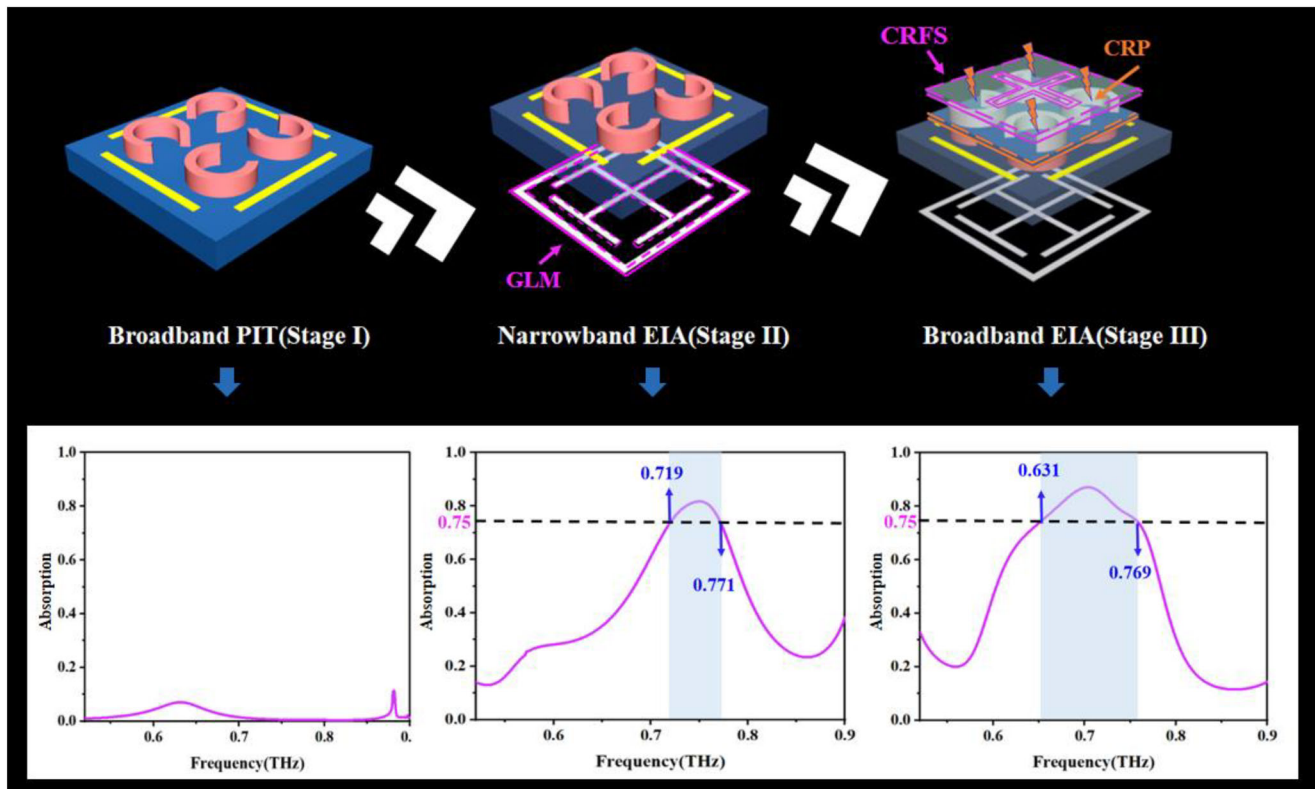


Figure 6. The three processes of broadband PIT to broadband EIA and the corresponding absorption curves.

coupling capacitance C_{m1} . The two resonant paths resonate at different frequencies, resulting in a standard Lorentz curve (see the two red dashed lines in Figure 5b). When the two paths interfere with each other, a transparent window of unit transmission coefficients appears in the amplitude spectrum (see the blue solid line in Figure 5b). To accommodate the simulation software requirements, the simulation circuit is simplified and the inter-resonator coupling effect is ignored. A comparison of the transmission response curve of the proposed PIT metastructure simulation with that of the circuit model theoretical analysis is given in Figure 5d. The fitted data are as follows: $R_1 = 2 \Omega$, $L_1 = 62 \text{ pH}$, $C_1 = 1.1 \text{ fH}$, $Z_1 = 50 \Omega$, $R_2 = 1 \Omega$, $L_2 = 78 \text{ pH}$, $C_2 = 0.41 \text{ fF}$, $Z_2 = 50 \Omega$. The two curves approximately overlap, verifying the validity of the given circuit model and the PIT metastructure. Some deviations may be due to some losses and complex coupling generated in the design.

2.4. Mechanistic Analysis of PIT to EIA

The proposed GMST based on the photosensitive material germanium can realize broadband PIT to EIA, which goes through three main design processes (see Figure 6), the first stage, as introduced above, through the near-field coupling between the localized plasmon resonance and the Mie resonance, realizing broadband PIT. In the second stage, a grid-like metastructure (GLM) is introduced to realize phase modulation, using three resonators coupled near-field to generate a magnetic dipole that strongly traps the incident magnetic energy, converting phase de-

structive interference to phase constructive interference, and realizing the conversion from broadband PIT to narrowband EIA. In the third stage, to enhance the EIA bandwidth, another layer of C-shaped reflection plate resonator (CRP) is introduced to increase the dark mode loss, and a layer of cross-shaped FSS resonator (CRFS) is also used. The dual effect effectively increases the EIA bandwidth. The absorption curves corresponding to each stage are also shown below the corresponding structure diagram (see Figure 6).

It has been reported that the methods of PIT to EIA are to increase the bright and dark mode coupling distance, reduce the bright mode radiation loss or increase the dark mode radiation loss,^[44] and the phase modulation achieved by constructive interference between multiple resonators has been proved to be the most effective way. And the key to achieving PIT to EIA in this paper is precisely the introduction of GLM. At this point, due to the near-field coupling between the three resonators to achieve magnetic resonance, the enhanced absorption peak at the resonant frequency will replace the narrow absorption depression accordingly, forming a good absorption resonance in the PIT window, thus realizing the transition from phase destructive interference to phase constructive interference. Its absorption rate exceeds 80% and the absorption peak frequency is located at 0.750 THz (see Figure 6, Stage II). To better explain the designed physical process, the simulated surface current distribution with phase difference for Stage II is plotted in Figure 7, where Figure 7a,b indicates $\varphi = 0.33 \pi$, 1.33π at the absorption peak (0.750 THz), respectively. It can be seen that the electric field in the TE mode is mainly localized in the radial

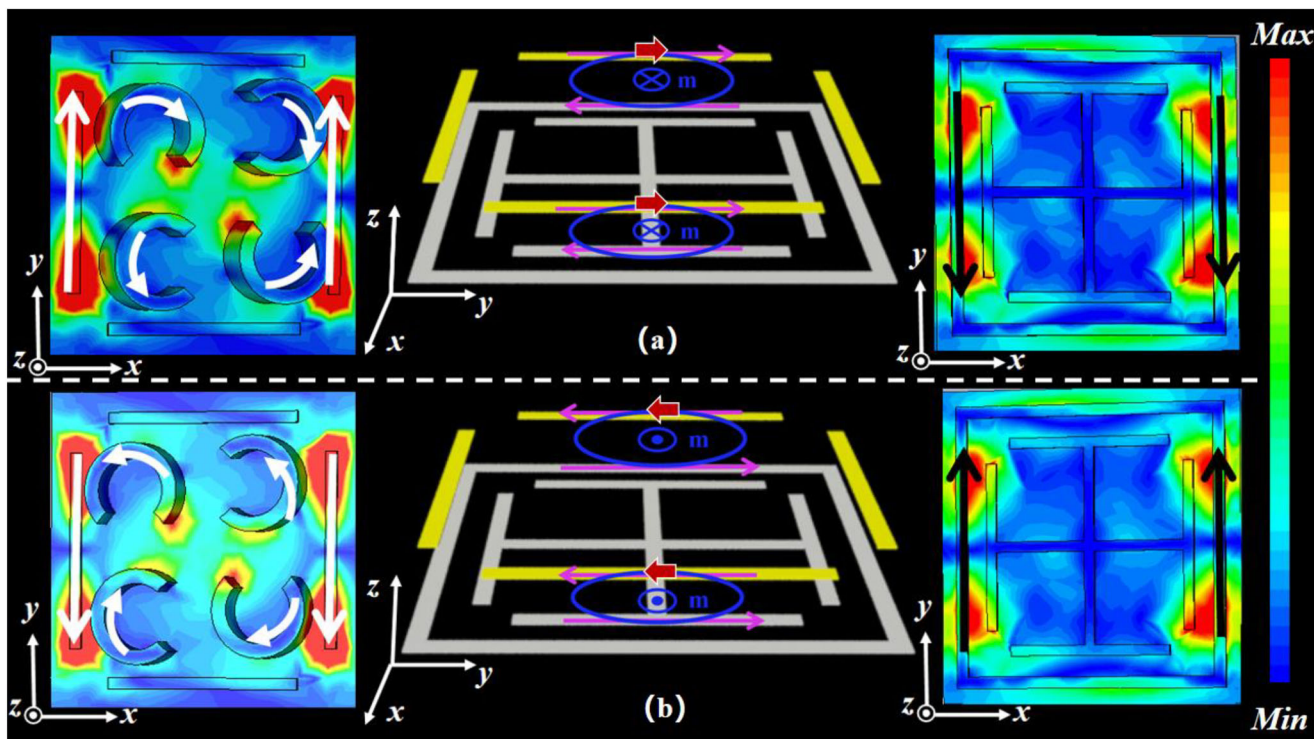


Figure 7. Narrowband EIA metastructure (Stage II) simulated surface current distribution at peak absorption frequency (0.750 THz) at TE mode, a) when $\varphi=0.33\pi$, and b) when $\varphi=1.33\pi$.

direction along the two gold cut wires in the electric field direction (y -axis) and on the two sides of the Ge “□” pattern directly below its vertical side. There is a π -phase difference between the surface currents on the two resonators, and the reverse current between them forms a magnetic dipole (see the blue circle in Figure 7). It can be determined by the right-hand rule that the direction m of the magnetic dipole is along the x -axis,^[47] which coincides with the direction of polarization of the incident magnetic field. Therefore, it strongly captures the incident magnetic energy, which causes a strong absorption.^[48] Therefore, by introducing GLM to achieve phase modulation, the constructive interference of the near-field coupling of the three resonators is used to generate a magnetic dipole, which strongly captures the incident magnetic energy and converts the phase destructive interference to phase constructive interference to achieve the PIT to EIA conversion.

To better explain the formation process of PIT to EIA, typical 4-level atomic systems in TE mode shown in **Figure 8a** are introduced, and EIA as the inverse process of PIT, the theory of simplicial energy levels in quantum is also applicable, where $|b\rangle$ and $|c\rangle$ are simply merged ground state energy levels and $|a\rangle$ and $|d\rangle$ are simply merged excited state energy levels. The difference from PIT is that, in addition to the introduction of coupling and detection light, additional control light that enables the jump from energy level $|c\rangle \rightarrow |d\rangle$ is required.^[49] And in different cases (e.g., in the coupling field, the Rabi frequency of the control field (which refers to the process by which an atom, when irradiated by a beam of coherent light, periodically absorbs a photon and re-emits it by excited emission, such that the reciprocal of a period is called the Rabi frequency) and the decay rate of the fourth

simplicial energy level do not coincide,^[50] the atomic coherence process of a four-energy level atomic system does not affect the medium absorption are the same, that is, the leap interaction between atoms is converted from phase destructive interference to phase constructive interference, specifically, the conversion of PIT to EIA. To achieve PIA while keeping the PIT effect stable and to integrate the PIT and EIA phenomena in the same metastructure, the GLM based on the photosensitive material Ge was introduced. The PIT to EIA conversion is achieved by multipath interference between the three resonators. The proposed metastructure has four gold cut wires corresponding to the energy level $|b\rangle \rightarrow |a\rangle$ leap, four C-shaped dielectric rings corresponding to the energy level $|a\rangle \rightarrow |c\rangle$ leap, and Ge GLM corresponding to the energy level $|c\rangle \rightarrow |d\rangle$ leap.

Figure 8b plots the EIA behavior in a three-branch series RLC resonator resonating at the detuned frequency. That is, a new branch RLC is added to the original PIT circuit model to represent the constructive interference effect of the GLM resonator. A series circuit is formed by the self-inductance L_{13} of the GLM, gap capacitor C_{13} and resistor R_{13} and connected to the original PIT structure through the coupling capacitor C_{m3} . A simplified simulation circuit to accommodate the circuit simulation software is also plotted in Figure 8b. And a comparison of the absorption of the narrowband EIA metastructure (Stage II) simulation with that of the circuit model theoretical analysis is shown in Figure 8c. The fitted data are as follows: $R_3 = 35\ \Omega$, $L_3 = 83\ \text{pH}$, $C_3 = 0.56\ \text{fF}$, $Z_1 = 30\ \Omega$, $Z_2 = 160\ \Omega$. The simulated and theoretical absorbance curves can be regarded as consistent. Some minor mismatches can be attributed to negligible capacitive/inductive coupling between resonators.

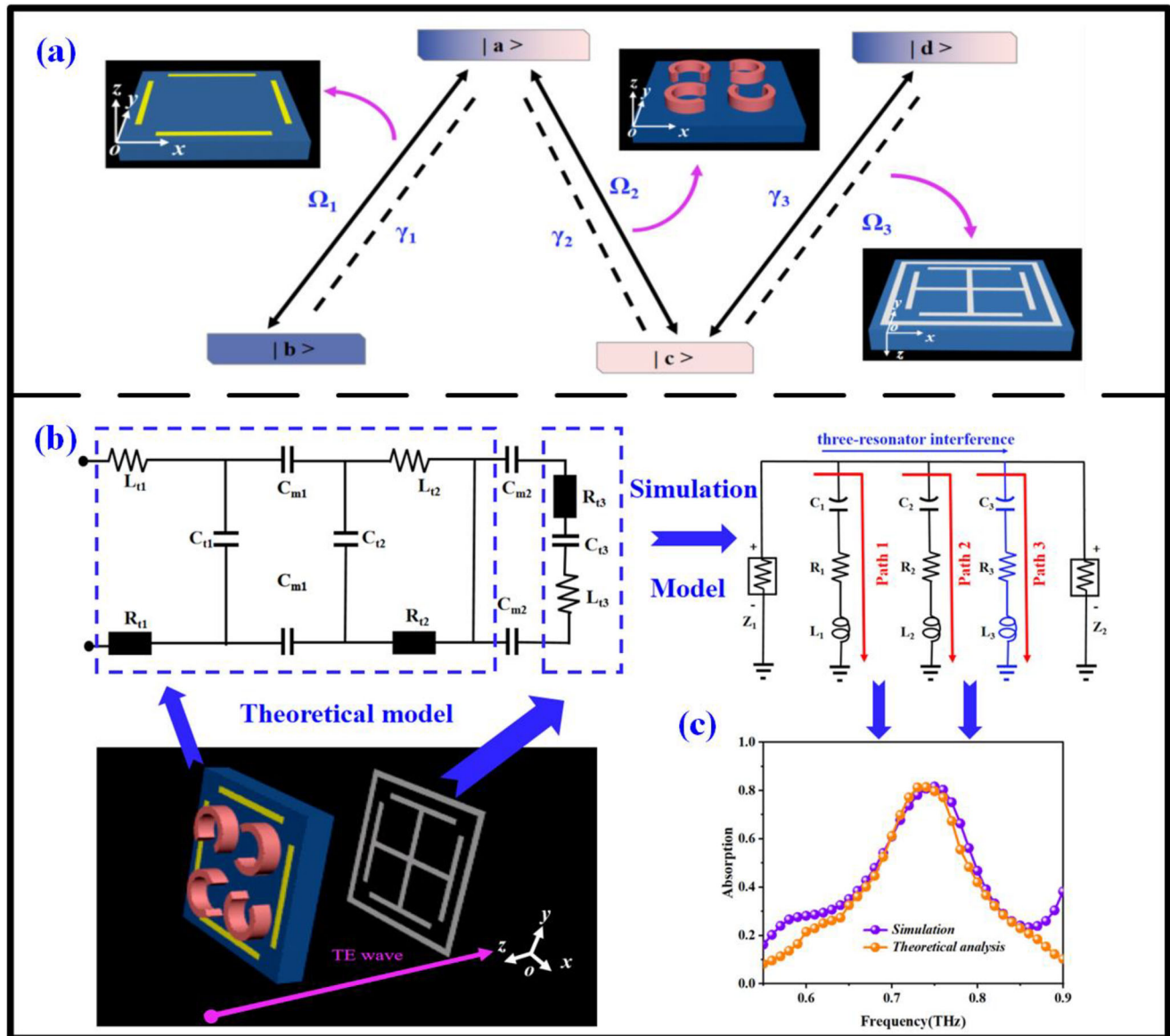


Figure 8. a) Explanation of the narrowband EIA phenomenon based on the 4-level atomic systems in TE mode, where Ω_1 , Ω_2 , Ω_3 are the Rabi frequencies of coupling light, detection light, and control light, respectively, and γ_1 , γ_2 , γ_3 are the rates of the three leapfrog channels at the rate of change of state.^[32] b) Explanation of the narrowband EIA phenomenon based on the circuit model, and c) comparison of the absorption of the narrowband EIA metastructure (stage II) simulation with that of the circuit model theoretical analysis.

2.5. Mechanistic Analysis of Broadband EIA

The next focus of this paper is the implementation of a broadband EIA, which has not been reported so far. Based on Stage II, the CRP metastructure is introduced and the individual resonance curves are shown in **Figure 9a**. The designed operating band corresponds to a reflector plate, which can also be considered as a band resistive surface. Placed above the four C-shaped dielectric rings (dark plasmon resonators), the Ge CRP exhibits a metallic state under illumination and the near-field coupling with the dark plasmon resonators enhances the loss of the dark plasmon resonators.^[44] Related experiments have shown that the coupling between attenuated radiation and dark modes can ef-

fectively transition the PIT to EIA, and this has been verified in the radiation spring oscillator model,^[34] which is homologous to either the generation of magnetic dipoles or the introduction of coupled phase detuning. Therefore, the introduction of the GMST species CRP proposed in this paper produces a phase constructive interference that eliminates the residual effect of the remaining phase destructive interference at the frequency point near the narrowband EIA and further enhances the broadband effect of the original absorption window, (indirectly attenuated phase destructive interference). In addition, the top layer of the proposed GMST is placed with a CRFS metastructure, a band-pass surface whose transmission response curve acting alone is shown in **Figure 9b**. The proposed GMST in this paper uses this

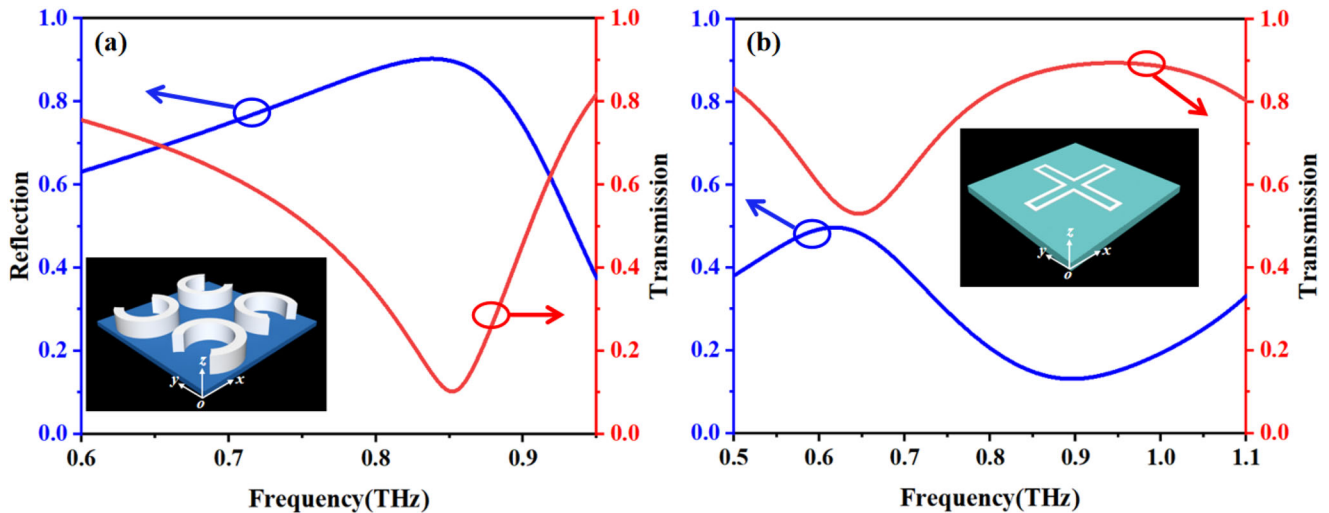


Figure 9. a) Transmission response curves (reflection and transmission curves) of CRP, and b) transmission response curves (reflection and transmission curves) of CRFS.

FSS to effectively modulate the electromagnetic wave transmission operating interval, enhance the transmission on both sides of the absorption peak (0.702 THz), and reduce the reflection of the structure, thus achieving an enhanced effect of bandwidth.

The bandwidth of EIA increases significantly under the dual action of CRP and CRFS, the variation of which has been plotted in **Figure 10**, while the effects of CPR and CRFS are reflected in the three curves of reflection, transmission as well as absorbance. The design idea is consistent with the simulated structure and also verifies the effectiveness of the increase in interference path and the introduction of FSS on increasing the bandwidth. It can also be understood that the near-field coupling between multiple resonators tends to form many interesting phenomena, and the broadband EIA formed by the designed GMST can also be seen as the formation of constructive interference between five resonators with no detuning frequencies, and as the interference path increases, the intensity of the phase constructive interference cancels out the residual energy of the nearby phase destructive interference, and forms in the working interval multiple absorption peak points are formed, resulting in a broadband effect.

The corresponding theoretical circuit model consists of five series RLC circuits resonating at detuned frequencies connected in parallel with each other (see **Figure 11a**), representing the roles of each of the five resonators, and the coupling between the resonators is represented by the coupling capacitance. One of the simplified simulation circuits to accommodate the simulation software is drawn in **Figure 11b**. The self-inductance L_{t4} , gap capacitor C_{t4} , and resistor R_4 of the CRP form a series circuit, which is connected in parallel with the self-inductance L_{t5} , gap capacitor C_{t5} , and resistor R_5 of the CRFS on the upper, and is coupled between the layers through C_{m4} . This part of the circuit is the key to EIA bandwidth increase, forming resonance near the original narrowband EIA band, thus increasing the bandwidth. Finally, we have carefully fitted the following data: $R_4 = 55 \Omega$, $L_4 = 75 \text{ pH}$, $C_4 = 0.8 \text{ fF}$, $R_5 = 80 \Omega$, $L_5 = 10 \text{ pH}$, $C_5 = 0.5 \text{ fF}$. The fitting results are shown in **Figure 11b**, which simulates the theoretical

analysis curve in agreement, with slight deviations within acceptable limits. This is attributed to the limitations of RLC resonance, and the neglect of other resonant modes. However, the model is still suitable for qualitative prediction of the effect of structural parameters on the resonant frequency which also confirms the rationality of the given GMST.

To systematically study the formation mechanism of broadband EIA, the metastructure forming narrowband EIA is seen as a monolithic Part I, while the two metastructures used to increase the bandwidth, CRP and CRFS, can be made as a monolithic Part II^[51] (see **Figure 11d**). Since the said Part I and Part II work in the EIA state when Ge is in the metallic state, the transmission coefficient is negligibly small and the conventional two-port network can be regarded as a single-port network. And it is well known that the complex single-port network can eventually be represented by an RLC series resonant circuit. The final simplified circuit is shown in **Figure 11d**. Thus, the proposed GMST can be approximated by two transmission line equivalent circuit models, and the geometrical parameters of the proposed GMST and the effects brought by Part II are discussed qualitatively and quantitatively. When the z -direction electromagnetic wave is incident, the gold cut wires and GLM form a magnetic dipole with strong magnetic resonance properties, which strongly captures the incident magnetic energy, and the C-shaped dielectric rings are excited with Mie resonance. According to the resonance theory of the equivalent RLC circuit, the mutual inductance effects within Part I and with Part II and the underlying structure can be described by L_{o1} and L_{o2} with the following equations, where μ_0 refers to the vacuum magnetic permeability^[52]

$$L_{o1} \approx 8\mu_0 r_1 w_3 l_3 \ln \left(2 \frac{h_1 + h_2}{(r_2 - r_1) \cdot w_4 \cdot l_4} \right) \quad (1)$$

$$L_{o2} \approx 4\mu_0 r_1 k_1 \ln \left(2 \frac{h_2 + h_3}{(r_2 - r_1) \cdot k_3} \right) \quad (2)$$

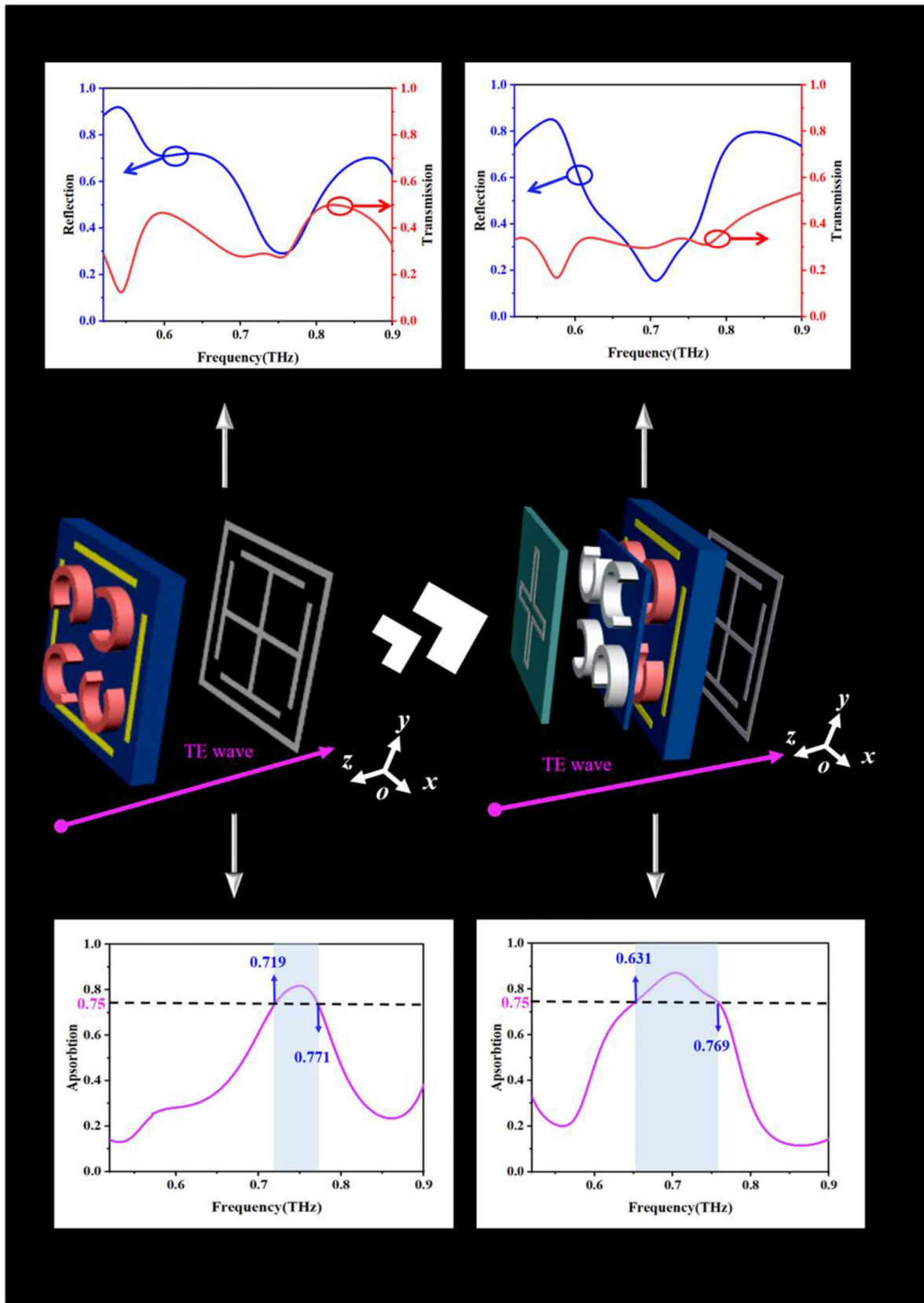


Figure 10. a) Narrowband EIA metastructure (Stage II) and its corresponding response curve (including reflection, transmission and absorption curves), and b) GMST (Stage III) and its corresponding response curve (including reflection, transmission and absorption curves).

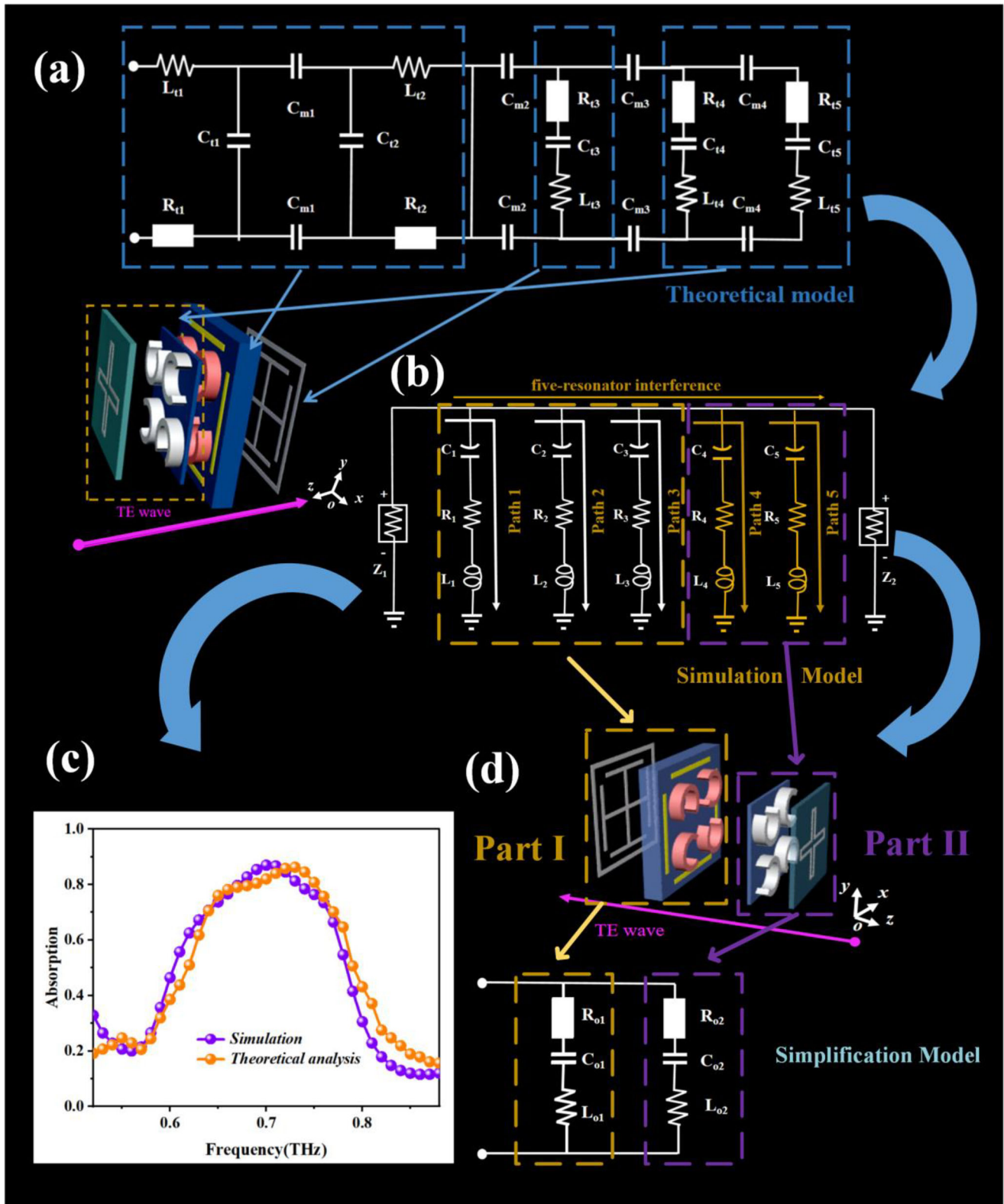


Figure 11. a) The explanation of the broadband EIA phenomenon based on the theoretical circuit model, b) simulation circuit model, c) comparison of the absorption of the broadband EIA metastructure (Stage III) simulation with that of the circuit model theoretical analysis, and d) simplification circuit model.

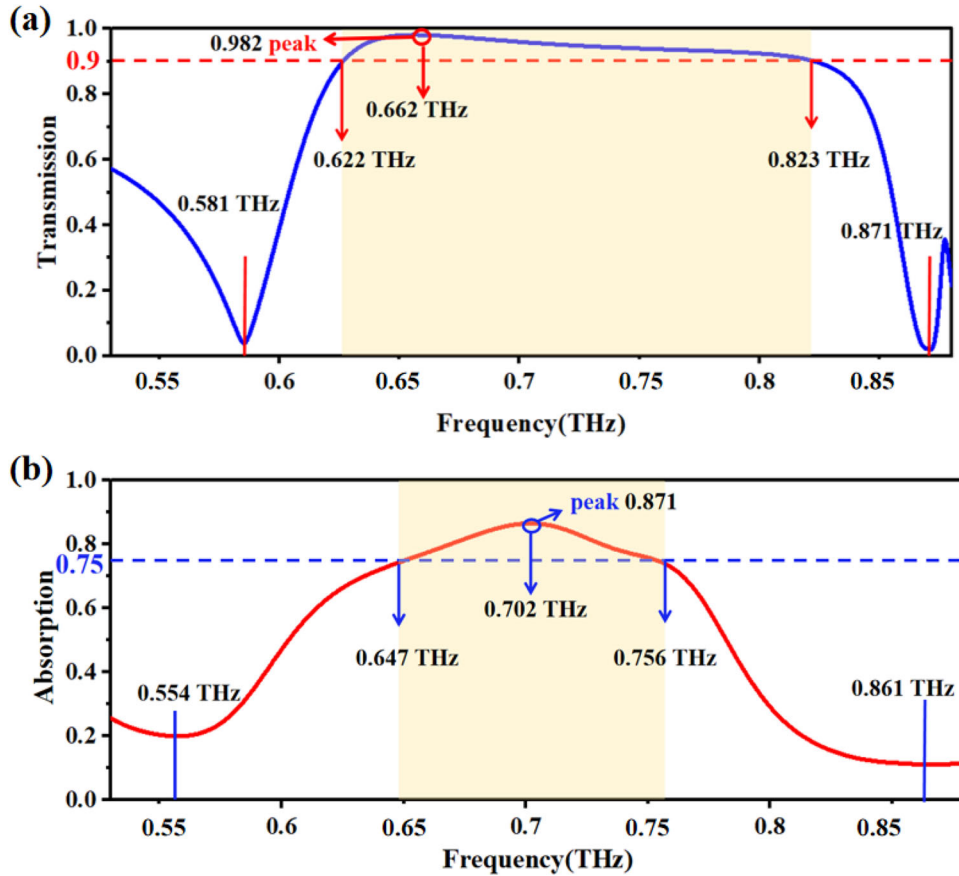


Figure 12. The two states of GMST, a) the transmission curve of GMST forming broadband PIT phenomenon when Ge conductivity is 0, and b) Absorption curve of GMST forming broadband EIA phenomenon when Ge conductivity is 1×10^6 .

The parallel plate capacitors C_{o1} and C_{o2} can be used to simulate the induced capacitance within Part I and between Part II and the underlying structure, as shown in Equations (3)–(4).

$$C_{o1} \approx \frac{\epsilon_r \epsilon_0 S_1}{h_1 + h_2} \quad (3)$$

$$C_{o2} \approx \frac{\epsilon_r \epsilon_0 S_2}{h_1 + h_2} \quad (4)$$

where ϵ_0 is the vacuum permittivity and ϵ_r is the relative permittivity of the dielectric substrate. S_1 and S_2 are the effective plane areas of Part I and Part II, respectively. Therefore, the resonant frequency ω_1 of Part I is represented by Equation (5), and the subsequent introduction of Part II will not only reconfigure the equivalent input impedance to match the space, but also the mutual coupling between Part II and Part I will trigger a new high-frequency resonance ω_2 . Thus, a new absorption peak is formed near the original narrow-band absorption frequency point to increase the EIA bandwidth.

$$\omega_1 = \frac{1}{2\pi \sqrt{L_{o1} C_{o1}}} \approx \frac{1}{2\pi \sqrt{\frac{8\mu_0 r_1 w_3 l_3 \epsilon_r \epsilon_0 S_1}{h_1 + h_2} \ln \left(2 \frac{h_1 + h_2}{(r_2 - r_1) \cdot w_4 \cdot l_4} \right)}} \quad (5)$$

$$\omega_2 = \frac{1}{2\pi \sqrt{L_{o2} C_{o2}}} \approx \frac{1}{2\pi \sqrt{\frac{4\mu_0 r_1 k_1 \epsilon_r \epsilon_0 S_2}{h_1 + h_2} \ln \left(2 \frac{h_2 + h_3}{(r_2 - r_1) \cdot k_3} \right)}} \quad (6)$$

3. Results and Discussion

3.1. The Two States of GMST

Above we analyzed the mechanism and response curves of bright and dark resonators forming PIT, and added three resonators based on the photosensitive material Ge to form broadband EIA, because of the special nature of the tunable Ge conductivity, a broadband PIT/EIA switchable metastructure was designed. When the Ge conductivity is 0, the GMST forms a peak PIT of 0.982 in the operating interval of 0.581 to 0.871 THz, where the wide transparency window above 0.9 covers from 0.622 to 0.823 THz with a relative bandwidth of 27.8% (see **Figure 12a**). It is worth proposing that even though the Ge conductivity is 0, there is still a slight effect on the PIT curve (Stage I) formed by the original dual resonator, but it does not prevent the formation of broadband PIT in the five-resonator system and the phenomenon is very good. When the light reaches a certain intensity, Ge takes on a metallic state with a conductivity of 1×10^6 ,^[41] at which time GMST forms an EIA with a peak value of 0.871 in the operating

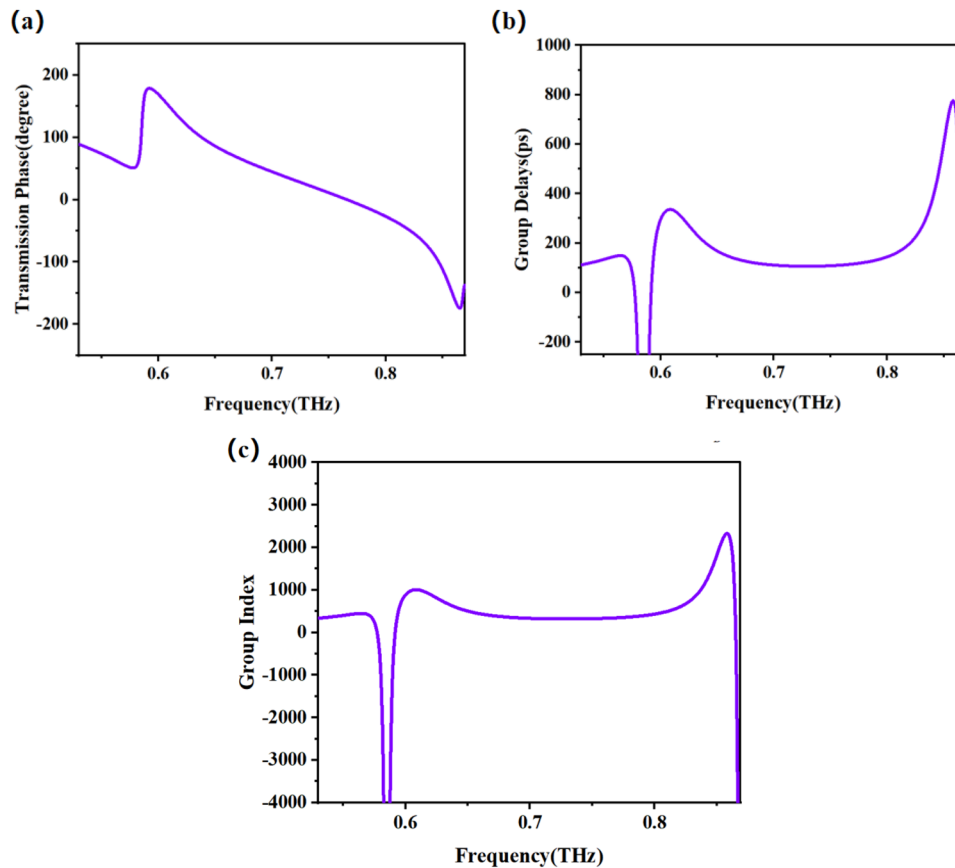


Figure 13. a) The transmission phase, b) the group delays, and c) the group index of the proposed GMST.

interval of 0.554 to 0.861 THz, where the wide absorption window above 0.75 covers from 0.647 to 0.756 THz with a relative bandwidth of 15.5% (see Figure 12b).

3.2. The Slow-Light Effect of PIT

An important property of the PIT phenomenon is the slow-light effect, which is widely used in the application of optoelectronic information devices. As a highly resonant phenomenon, PIT significantly slows down the incident electromagnetic wave velocity in opaque media, while greatly exacerbating the dispersion variation. In the transparent window of PIT, the drastic phase shift directly triggers a high group delay (GD), while the phase shift time is positively correlated with the local field enhancement and is an important factor to verify the induced optical state. In addition, the corresponding group index (GI) is used to describe the slow wave effect in the proposed GMST. The calculation is based on the following^[53]

$$\tau_{GD} = -\frac{\partial\varphi}{\partial\omega} \quad (7)$$

$$n_{GI} = \frac{c}{t}\tau_{GD} \quad (8)$$

where ω , φ , c , and t denote the angular frequency, the transmission phase, the speed of light in a vacuum, and the total thickness

of the proposed GMST, respectively. Thus, the phase of the incident wave in **Figure 13a** shows two abrupt changes on both sides of the PIT transmission window, which is consistent with a typical PIT. **Figure 13b** shows clearly that the TE mode has a maximum GD of 776 ps, corresponding to a maximum GI of 2326 (see **Figure 13c**). As a result, the transmission spectrum has a strong dispersion and low loss, while the associated dispersion has a distinct phase spectrum, showing a clear slow light effect. It has a wide range of applications in optical switching, enhanced nonlinear effects, and optical storage.

3.3. Key Parameters Impact Analysis

To further investigate the dependence of the proposed GMST on the incidence angle, the transmission and absorption efficiencies at different incidence angles are depicted in **Figure 14a,b**, respectively. It can be seen that the EIT still shows broadband transmission at an incidence angle of less than 20°, while the frequency band of transmission above 0.9 gradually decreases until it disappears as the incidence angle increases. The EIA also shows the same trend, the frequency band above 0.75 is still very wide when the incidence angle is within 30°, then as the incidence angle increases, the absorption spectrum suffers a certain degree of attenuation and gradually turns into the narrow band absorption and blue shift phenomenon. This phenomenon can be explained

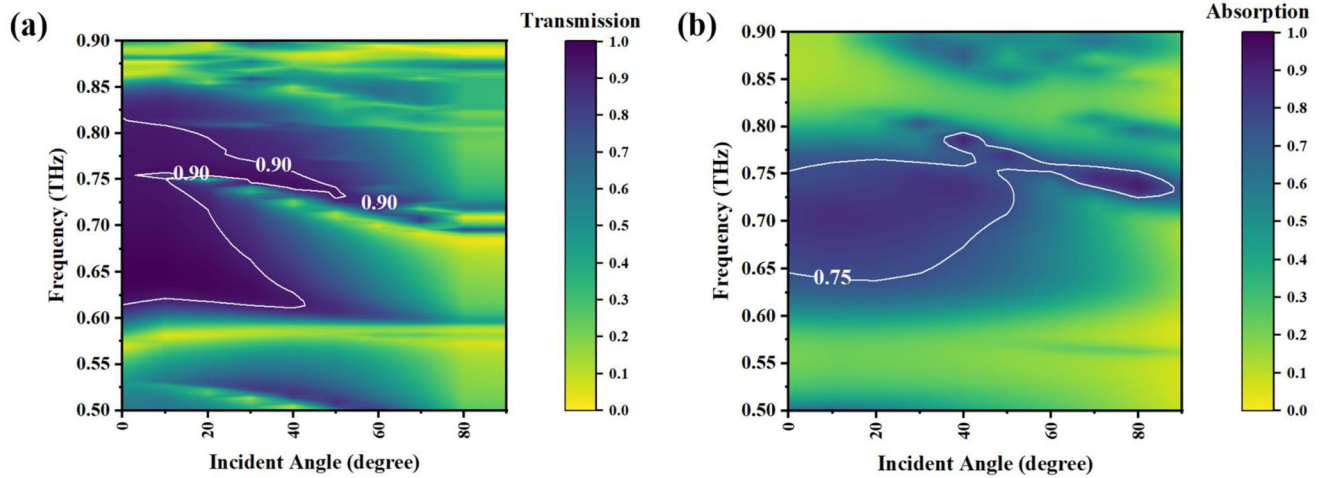


Figure 14. a) The transmission and b) the absorption at different incident angles (varying from 0° to 90°) for the TE mode.

by the fact that as the incident angle increases, the electric field components of the electromagnetic waves arrive at different resonant structures at different times, thus showing differences in the modulation effect on the electromagnetic waves. However, in short, the proposed GMST can still present a broadband EIT/EIA effect with some stability under the action of small incidence angles.

To obtain the best phenomena, the geometrical parameters of the proposed GMST were optimized by simulation software. The performance variation curves of two key parameters are presented in **Figure 15**, which include the coupling distance h_1 between the dual resonator structure forming the PIT and the underlying GLM metastructure, the thickness and inner radius size of the four C-shaped dielectric rings d_3 and r_1 . Observing **Figure 15a,b**, it can be seen that the absorbance curve is red-shifted as h_1 increases, and the two transmission valleys, as well as the relative bandwidth, have the best effect at $h_1 = 32 \mu\text{m}$, which is because the coupling distance h_1 between the dual resonator structure forming the PIT is the key parameter that affects the conversion of phase destructive interference into phase constructive interference, that is, it has a greater effect on EIA. At the same time, h_1 also affects the PIT to some extent, and as h_1 increases, the transmission curve appears red-shifted, which is because of the red-shift of the operating frequency caused by the increase of the dielectric substrate thickness. As can be seen in **Figure 15c**, with the increase in the thickness of the CPR and four C-shaped dielectric rings d_3 , the transmission window is significantly compressed and the transmission amplitude in the high-frequency region is optimized. This is attributed to the enhancement of the Mie resonance effect of the dark plasmon resonator. At the same time, with the increase of d_3 , the absorbance curve shows a significant red-shift and a general trend of narrowing the bandwidth, and the d_3 is finally selected as $27 \mu\text{m}$ considering the specific effects (see **Figure 15d**). Moreover, considering that thickness uniformity is usually an issue in the deposition process, the inner radius size of the four C-shaped dielectric rings r_1 is discussed in **Figure 15e,f**. As the gradient thickness of walls in C-shaped dielectric rings increases, the right transmission valley and bandwidth above 0.9 of the transmission curve are both improved. But

this is at the expense of the two absorption valleys of the absorption curve of the EIA. Therefore, the adjustment of specific geometric parameters has a certain effect on the change of the operating band.

To further validate the proposed mechanism of broadband EIA formation of GMST, the impedance matching principle is introduced as a classical theory. It is assumed that the equivalent impedance (Z) of the proposed integrated device is numerically close or even equivalent to the equivalent impedance (Z_0) in free space, and thus the absorption performance is improved. To check the degree of impedance matching of Z and Z_0 , the normalized complex impedance $Z_r = Z/Z_0$ is introduced. Z_r can be obtained by inversion of the S-parameters as^[44]

$$Z_r = \sqrt{\frac{(1 + S_{11}(\omega))^2 - S_{21}(\omega)^2}{(1 - S_{11}(\omega))^2 - S_{21}(\omega)^2}} \quad (9)$$

where $S_{11}(\omega)$ and $S_{21}(\omega)$ refer to the scattering parameters of reflection and transmission, respectively. Perfect absorption can be achieved when the real and imaginary parts of Z_r converge to 1 and 0, respectively. The real and imaginary parts of Z_r calculated from the s-parameters of the optimized GMST as a function of frequency are shown in **Figure 16**. In the 0.55–0.75 THz range, the normalized input impedance of Z_r is slightly above 1 in the real part and close to 0 in the imaginary part, leading to an effective broadband absorption, an observation that confirms a perfect match with free space.

4. Conclusion

In conclusion, a GMST with switching features from broadband PIT to EIA is studied theoretically in various aspects. GMST forms a broadband PIT through the near-field coupling between the localized plasmon resonance and the Mie resonance employing four gold cut wires as bright plasmon resonators and four C-shaped dielectric rings as dark plasmon resonators. A wide transparent window above 0.9 is achieved covering from 0.622

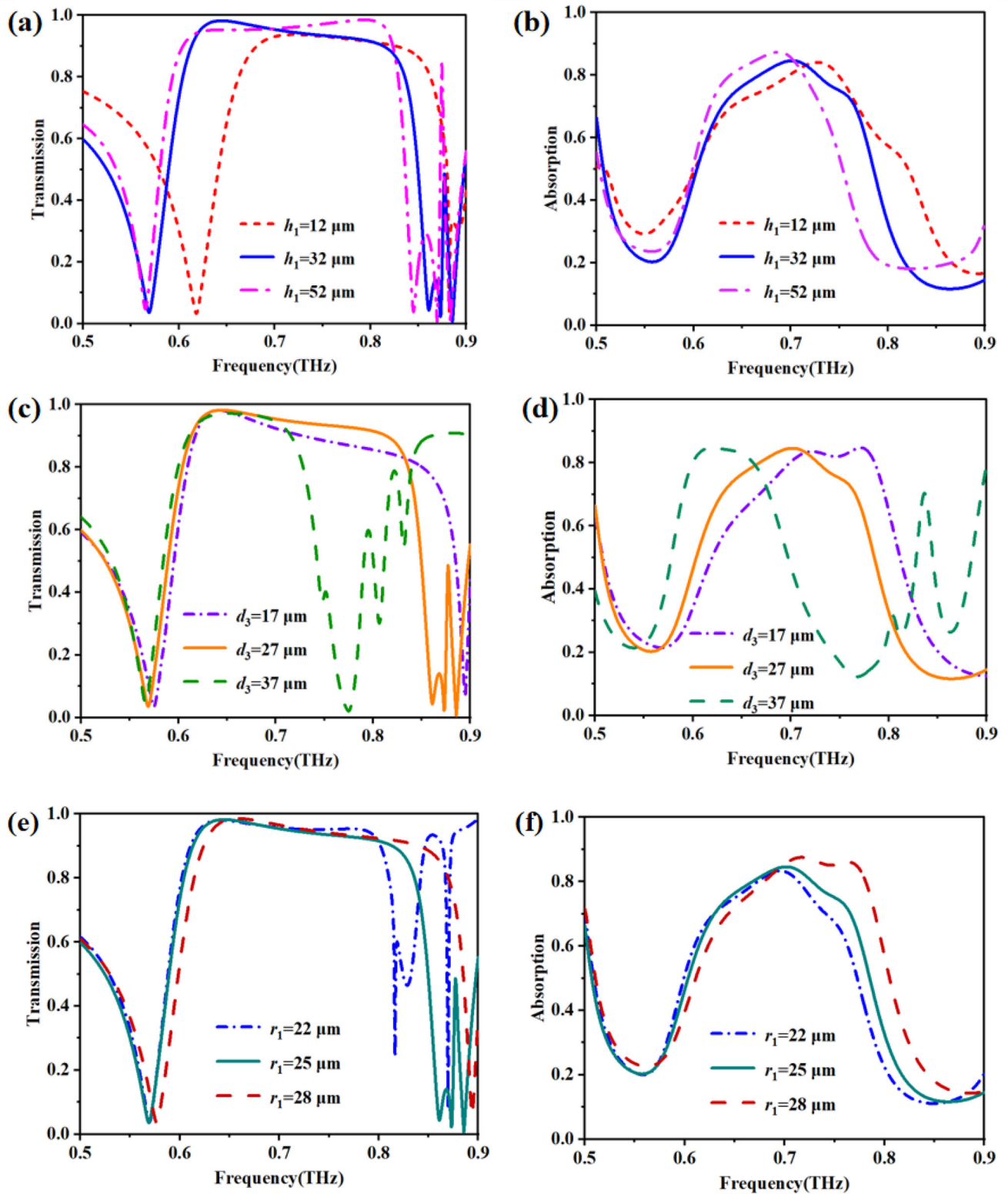


Figure 15. The calculated a) transmission, and b) absorption curves when h_1 varies from 12 to 52 μm . The results of c) transmission, and d) absorption curves when d_3 differs from 17 to 37 μm . The results of e) transmission, and f) absorption curves when r_1 differs from 22 to 28 μm .

Received: August 31, 2022
Revised: October 31, 2022
Published online:

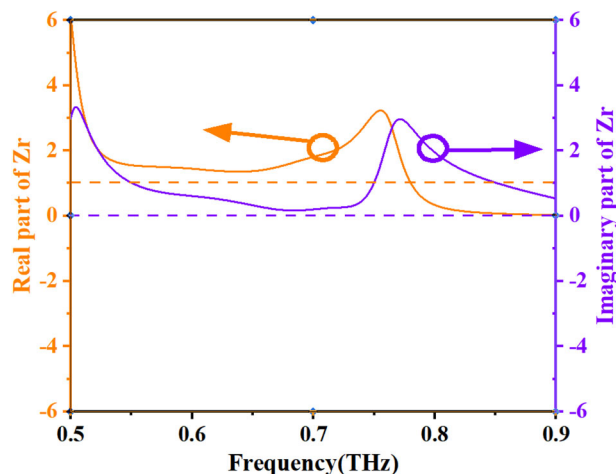


Figure 16. The normalized complex impedance Z_r of the final optimized GMST for the TE wave.

to 0.823 THz with a relative bandwidth of 27.8%. In addition, through phase modulation, a magnetic dipole is generated by the constructive interference of the near-field coupling of the three resonators, which strongly captures the incident magnetic energy and converts the phase destructive interference into phase constructive interference to realize the PIT to EIA conversion. In addition, another layer of reflection plate composed of CRP is introduced to increase the dark mode loss, and a layer of FSS, increases the bandwidth of EIA. A wide absorption window above 0.75 is achieved covering from 0.647 to 0.756 THz with a relative bandwidth of 15.5%. In the end, the surface current as well as the atomic energy level diagram is introduced to explain the operating principle of GMST, and the PIT and EIA phenomena are reproduced using the circuit model, confirming the consistency and validity of the simulation and theory.

Acknowledgements

This work was supported by the National College Student Innovation Training Program (Grant No. 202210293014Z), and College Student Innovation Training Program of Nanjing University of Posts and Telecommunications.

Conflict of Interest

The authors declare no conflict of interest.

Data Availability Statement

The data that support the findings of this study are available on request from the corresponding author. The data are not publicly available due to privacy or ethical restrictions.

Keywords

circuit model, electromagnetically induced absorption, electromagnetically induced transparency, frequency selective surfaces, plasmon-induced transparency

- [1] B. Gerislioglu, A. Ahmadiwand, N. Pala, *Phys. Rev. B* **2018**, *97*, 161405.
- [2] R. T. Ako, A. Upadhyay, W. Withayachumnankul, M. Bhaskaran, S. Sriram, *Adv. Opt. Mater.* **2020**, *8*, 1900750.
- [3] A. Ahmadiwand, B. Gerislioglu, R. Ahuja, Y. K. Mishra, *Mater. Today* **2020**, *32*, 108.
- [4] X. J. Fu, F. Yang, C. X. Liu, X. J. Wu, T. J. Cui, *Adv. Opt. Mater.* **2020**, *8*, 1900628.
- [5] L. Zeng, H. F. Zhang, *IEEE Sens. J.* **2022**, *22*, 224.
- [6] M. Amin, R. Ramzan, O. Siddiqui, *Sci. Rep.* **2018**, *8*, 2357.
- [7] M. F. Limonov, M. V. Rybin, A. N. Poddubny, Y. S. Kivshar, *Nat. Photonics* **2017**, *70*, 543.
- [8] C. J. Gao, D. Zhang, H. F. Zhang, *Phys. E* **2022**, *144*, 115225.
- [9] L. Zeng, T. Huang, G. B. Liu, H. F. Zhang, *Opt. Commun.* **2019**, *436*, 7.
- [10] S. E. Harris, *Phys. Today* **1997**, *50*, 36.
- [11] M. Fleischhauer, A. Imamoglu, J. P. Marangos, *Rev. Mod. Phys.* **2005**, *77*, 633.
- [12] E. Distante, P. Farrera, A. Padrón-Brito, *Nat. Commun.* **2017**, *8*, 14072.
- [13] A. K. Osgouei, H. Hajian, A. E. Serebryannikov, E. Ozbay, *J. Phys. D: Appl. Phys.* **2021**, *54*, 275102.
- [14] B. Wu, J. Hulbert, E. Lunt, *Nat. Photonics* **2010**, *4*, 776.
- [15] A. Safavi-Naeini, T. Alegre, J. Chan, *Nature* **2011**, *472*, 69.
- [16] Y. Q. Li, M. Xiao, *Opt. Lett.* **1995**, *20*, 1489.
- [17] J. Dhanya, A. V. Basiluddeen, R. Ratheesh, *Scr. Mater.* **2017**, *132*, 1.
- [18] V. Erçaglar, H. Hajian, E. Özbay, *J. Phys. D: Appl. Phys.* **2021**, *54*, 245101.
- [19] D. R. Smith, J. B. Pendry, M. C. Wiltshire, *Science* **2004**, *305*, 788.
- [20] J. Valentine, S. Zhang, T. Zentgraf, E. Ulin-Avila, D. A. Genov, G. Bartal, X. Zhang, *Nature* **2008**, *455*, 376.
- [21] A. Ahmadiwand, B. Gerislioglu, R. Ahuja, Y. K. Mishra, *Laser Photonics Rev.* **2020**, *14*, 1900326.
- [22] B. Gerislioglu, G. Bakan, R. Ahuja, J. Adam, Y. K. Mishra, A. Ahmadiwand, *Mater. Today Phys.* **2020**, *12*, 100178.
- [23] L. Zeng, H. F. Zhang, *Ann. Phys.* **2022**, *534*, 2100462.
- [24] C. Wu, A. B. Khanikaev, G. Shvets, *Phys. Rev. Lett.* **2011**, *106*, 107403.
- [25] B. Wang, P. Yu, W. Wang, X. Zhang, H. C. Kuo, H. Xu, Z. M. Wang, *Adv. Opt. Mater.* **2021**, *9*, 2001520.
- [26] A. D. Utyushev, V. I. Zakomirnyi, I. L. Rasskazov, *Rev. Phys.* **2021**, *6*, 100051.
- [27] H. Zhu, X. Jing, P. Zhou, *Superlattices Microstruct.* **2018**, *113*, 592.
- [28] Q. Zhao, J. Zhou, F. Zhang, D. Lippens, *Mater. Today* **2009**, *12*, 60.
- [29] A. A. Basharin, M. Kafesaki, E. N. Economou, C. M. Soukoulis, V. A. Fedotov, V. Savinov, N. I. Zheludev, *Phys. Rev. X* **2015**, *5*, 011036.
- [30] E. Semouchkina, R. Duan, G. Semouchkin, R. Pandey, *Sensors* **2015**, *15*, 9344.
- [31] P. Ding, J. He, J. Wang, C. Fan, E. Liang, *Appl. Opt.* **2015**, *54*, 3708.
- [32] A. Lezama, S. Barreiro, A. M. Akulshin, *Phys. Rev. A* **1999**, *59*, 4732.
- [33] M. Y. Cao, T. L. Wang, H. Y. Zhang, Y. P. Zhang, *Opt. Commun.* **2018**, *413*, 73.
- [34] P. Tassin, L. Zhang, R. K. Zhao, A. Jain, T. Koschny, C. M. Soukoulis, *Phys. Rev. Lett.* **2012**, *109*, 187401.
- [35] M. L. Wan, J. N. He, Y. L. Song, F. Q. Zhou, *Phys. Lett. A* **2015**, *379*, 1791.
- [36] N. Xu, M. Manjappa, R. Singh, W. Zhang, *Adv. Opt. Mater.* **2016**, *4*, 1179.
- [37] R. Taubert, M. Hentschel, J. Kästel, H. Giessen, *Nano Lett.* **2012**, *12*, 1367.

- [38] L. Verslegers, Z. C. Ruan, P. B. Catrysse, S. H. Fan, *Phys. Rev. Lett.* **2012**, *108*, 083902.
- [39] W. Li, Y. Wang, S. Sun, X. Shi, *IEEE Access* **2020**, *8*, 23904.
- [40] Y. Deng, Z. Song, *Opt. Mater.* **2020**, *105*, 109972.
- [41] Z. H. Guo, Y. Z. Sun, L. Zeng, H. F. Zhang, *Ann. Phys.* **2022**, *534*, 2100499.
- [42] W. Wei, Y. Xin, S. Bing, Z. Xia, *Nanoscale Res. Lett.* **2019**, *14*, 246.
- [43] M. N. Afsar, H. Ding, *IEEE Trans. Instrum. Meas.* **2001**, *50*, 402.
- [44] Y. Z. Sun, C. J. Gao, J. Qu, H. F. Zhang, *Ann. Phys.* **2022**, *534*, 2200130.
- [45] M. D. Eisaman, A. André, F. Massou, *Nature* **2006**, *438*, 837.
- [46] N. Jin, J. S. Li, *Microw. Opt. Technol. Lett.* **2009**, *17*, 18590.
- [47] X. Zhang, N. Xu, K. Qu, Z. Tian, R. Singh, J. Han, G. S. Agarwal, W. Zhang, *Sci. Rep.* **2015**, *5*, 10737.
- [48] V. A. Fedotov, M. Rose, S. L. Prosvirnin, N. Papasimakis, N. I. Zheludev, *Phys. Rev. Lett.* **2007**, *99*, 147401.
- [49] A. V. Taichenachev, A. M. Tumaikin, V. I. Yudin, *Phys. Rev. A* **2000**, *61*, 011802.
- [50] A. M. Kulshin, S. Barreiro, A. Lezama, *Phys. Rev. A* **1998**, *57*, 2996.
- [51] Y. G. Zhang, J. B. Wu, L. J. Liang, G. C. Zhou, B. B. Jin, Y. J. Feng, *Sci. China Inf. Sci.* **2014**, *57*, 1.
- [52] R. Mishra, R. Panwar, *Opt. Quantum Electron.* **2020**, *52*, 317.
- [53] H. Lu, X. Liu, D. Mao, *Phys. Rev. A* **2012**, *85*, 053803.